Locally-Rank-One-Based Joint Unmixing and Demosaicing Methods for Snapshot Spectral Images. Part II: a Filtering-Based Framework

Kinan Abbas, Matthieu Puigt, Gilles Delmaire, Gilles Roussel

Authors' final version of a paper published in "IEEE Transactions on Computational Imaging"

Paper reference: K. Abbas, M. Puigt, G. Delmaire and G. Roussel, "Locally-Rank-One-Based Joint Unmixing and Demosaicing Methods for Snapshot Spectral Images. Part II: A Filtering-Based Framework," in IEEE Transactions on Computational Imaging, vol. 10, pp. 806-817, 2024.

IEEE online version: `https://dx.doi.org/10.1109/TCI.2024.3402441`.

Note: The version of this paper published by the Editor contains one typo which is corrected in this authors' final version:

– In Eq. (5), the variable on the left side of the equal sign should be $x_i(\lambda_i)$ (instead of $y_i(\lambda_i)$ in the published version). As a consequence, this equation reads

$$x_i(\lambda_i) = \sum_{l=1}^{p} g_{il} \left(\sum_{j=1}^{k} h_i(\lambda_j) \cdot f_l(\lambda_j) \right) + \omega_i$$

instead of

$$y_i(\lambda_i) = \sum_{l=1}^{p} g_{il} \left(\sum_{j=1}^{k} h_i(\lambda_j) \cdot f_l(\lambda_j) \right) + \omega_i.$$

Locally-Rank-One-Based Joint Unmixing and Demosaicing Methods for Snapshot Spectral Images. Part II: a Filtering-Based Framework

Kinan Abbas, *Student Member, IEEE,* Matthieu Puigt, *Member, IEEE,* Gilles Delmaire, and Gilles Roussel

***Abstract*—This paper presents novel unmixing and demosaicing methods for snapshot spectral imaging (SSI) systems utilizing Fabry-Perot filters. Unlike conventional approaches that perform unmixing after image restoration or demosaicing, our proposed methods leverage Fabry-Perot filter deconvolution and extend the "pure pixel" framework to the SSI sensor patch level, enabling improved unmixing accuracy and introducing the concept of localized spectral purity. Through extensive experimentation on synthetically generated data and real images captured by SSI cameras, we demonstrate the superiority of our methods over state-of-the-art techniques. Furthermore, our results showcase the effectiveness of the proposed approach over our recently proposed joint unmixing and demosaicing method based on low-rank matrix completion.**

***Index Terms*—Snapshot Spectral Imaging, Unmixing, Demosaicing, Low-Rank Approximation, Sparsity, Deconvolution.**

I. Introduction

SNAPSHOT spectral imaging (SSI) is a technique used in hyperspectral imaging (HSI) that aims to acquire spectral information from a scene by associating each spatial pixel with a specific spectral band [1]. Traditionally, HSI involves wavelength-scanning, point-scanning, or line-scanning methods, which require repetitive measurements and can be time-consuming. Recent advancements have introduced snapshot spectral cameras that employ Fabry-Perot filters (FPf) or compressive coded-aperture snapshot spectral imagers (CASSI) to overcome these limitations. In this study, our focus is on snapshot mosaic cameras using Fabry-Perot filter technology [2], [3]. Fabry-Perot filters (FPf) are widely used for spectral filtering in optical systems. Snapshot mosaic cameras incorporate FPf monolithically on CMOS image sensors, allowing for decreased stray light, increased sensitivity, and faster acquisition times. The filters in these cameras are designed with varying cavity lengths for each pixel in a filter cell, arranged in a mosaic pattern replicated across the sensor surface as shown in Fig. 1. This per-pixel layout enables the capture of a complete scene without the need for image duplication. Unlike traditional scanning methods, snapshot mosaic cameras offer several advantages, including fast acquisition times, compact size, and portability. However, they present a trade-off between spatial and spectral resolution due to the association of each pixel with a specific spectral band. In particular, the SSI camera manufacturer provides a pipeline to process such data, which includes an important stage known as "demosaicing". Traditional demosaicing techniques utilize spatial and/or spectral correlation and use methods such as Weighted Bilinear interpolation (WB) [4], Iterative Spectral Difference (ItSD) [5], pseudo-panchromatic image (PPID) [6], Binary Tree-Based Generic Demosaicing (BTES) [7], graph-regularized low-rank matrix completion (GRMR) [8], as well as structural and adaptive nonlocal optimization (SaND) [9]. Recently deep learning methods have emerged as alternatives [10]–[13].

After the 3-D hyperspectral image has been reconstructed from the 2-D SSI data, we can employ any post-processing technique of choice. In particular, the unmixing process that involves extracting the spectral signatures of all the endmembers which are present in an observed scene. Specifically, popular unmixing methods operate under the assumption that for each endmember, there is at least one spatial pixel where the corresponding material exclusively exists. This implies that the observed spectrum in such a pixel matches the endmember spectrum. The most widely used algorithms are the vertex component analysis (VCA) [14], N-FINDR [15], the pixel purity index (PPI), and the sequential maximum angle convex cone (SMACC) [16]. Sparse component analysis (SCA) is one of the main approaches to Blind Source Separation (BSS). It detects single-source zones by exploiting the source sparsity properties in different representation domains [17]. They are categorized into 1-sparse and q-sparse methods (with $q \geq 2$) [18], [19].

In the first part of this paper [20], we investigated the behavior of joint demosaicing and unmixing methods for snapshot spectral imaging (SSI) systems. In addition to a naive approach—straightforwardly derived from Weighted Nonnegative Matrix Factorization (WNMF)—we proposed two novel demosaicing methods, i.e., KPWNMF (K-means Patch-based Weighted Nonnegative Matrix Factorization) and VPWNMF (VCA Patch-based Weighted Nonnegative Matrix Factorization). These methods incorporated the assumption of sparse abundances within sensor "patches," where a single endmember primarily dominates each patch. The methods employed rank-1 WNMF computations, a specialized single-source confidence measure, endmember extraction, and abundance estimation. However, they diverged in treating scenarios involving multiple endmembers, providing distinct solutions to address such cases. We demonstrated that starting the

K. Abbas, M. Puigt, G. Delmaire, and G. Roussel are with Univ. Littoral Côte d'Opale (ULCO), LISIC – UR 4491, F-62219 Longuenesse, France, e-mail: firstname.lastname@univ-littoral.fr.

This work was partly funded by the Région Hauts-de-France. Experiments presented in this paper were carried out using the CALCULCO computing platform, supported by SCoSI/ULCO.

unmixing process directly from the raw images yields superior unmixing and demosaicing enhancements. Building upon this finding, in this second part of the paper, we deeper analyze the pipeline to restore the HSI data cube and we explore the utilization of the harmonic response matrix of Fabry-Perot filters (FPf) for joint unmixing and deconvolution. Our objective is to showcase that the integration of joint unmixing and deconvolution techniques leads to enhanced unmixing and demosaicing outcomes compared to the joint demosaicing and unmixing approaches, as well as the traditional 2-stage methods involving separate demosaicing and unmixing steps.

Furthermore, the current image processing pipeline of snapshot images involves applying a correction matrix after demosaicing in order to remove some unwanted harmonics. In contrast, our proposed approaches obviate the need for applying the correction matrix and initiates the deconvolution process directly from the raw SSI image. Through this novel methodology, we aim to demonstrate the efficacy of our approaches in achieving improved unmixing and demosaicing results while simplifying the overall processing pipeline.

To evaluate the performance of the proposed methods, we accomplish experiments on SSI simulations derived from synthetic images. Additionally, we process real SSI images taken from Hyko 2 dataset [21].

It should be noticed that a preliminary version of this work was published in [22], where one of our proposed methods was introduced. However, this paper differs from [22] as follows. We propose a second approach using different abundance assumptions. Moreover, while the work in [22] mainly focused on the endmember estimation, we here also explore the abundance estimation and investigate both the demosaicing and unmixing enhancement of our proposed methods.

The remainder of the paper is organized as follows. Section II presents the snapshot images processing pipeline and the related work in deconvolution for hyperspectral imaging. We then introduce the joint unmixing and deconvolution problem in Section III. Section IV introduces our proposed methods, whose performances are investigated in Section V. Finally, we conclude our discussion and introduce future directions for research in Section VI. A table of notations used throughout this paper is provided in Table I for clarity and ease of understanding.

TABLE I
TABLE OF MATHEMATICAL NOTATIONS

Notation	Description
Y	Matrix
$\hat{Y}$	Estimated Y matrix
$\mathbb{H}$	Scaled convolution matrix
$\underline{g}$	Column vector
g_{il}	the (i,l)-th element of G
$\circ$	Hadamard product
f	Row vector
y^T	Transpose of the vector y
$\|\cdot\|_F^2$	The Frobenius norm
$\approx$	Approximately equal
$\|\cdot\|_2^2$	Squared Euclidean Norm
$\gg$	Much greater than
$\triangleq$	Is defined as or is equivalent to
$\mathbb{F}, \mathbb{X}$	Pool of the spectra

Fig. 1. The SnapShot SWIR camera from IMEC using a mosaic pattern of 16 SWIR filters (Source IMEC).

II. RELATED WORK

In order to fully exploit the advantages of snapshot spectral imaging and derive precise and reliable information from the acquired data, several essential processing steps must be undertaken. These processing stages, including demosaicing, spectral correction, and unmixing, play a critical role in refining the hyperspectral data's quality, spatial resolution, and interpretability. Given our introduction of demosaicing and unmixing in the first part of this paper [20], in this discussion, we delve into the significance and methodologies of spectral correction and deconvolution, highlighting their impact on harnessing the benefits of SSI imaging and enabling the analysis of hyperspectral data.

Since SSI cameras associate each spatial pixel with a specific spectral band—thus introducing a critical trade-off between spatial and spectral resolution—a post-processing technique known as "demosaicing" must be applied to estimate the entire HS data cube and conserve the spatial resolution. The straightforward method for generating the entire hyperspectral cube from a single snapshot image involves grouping the suitable number of pixels with a corresponding reduction in spatial resolution. Nonetheless, demosaicing aims to create the complete hyperspectral (HS) data cube and preserve the spatial resolution. To achieve this, several techniques have been proposed to estimate the missing information, which can be classified into "traditional" methods and deep learning-based strategies. Most demosaicing methods—including our joint unmixing and demosaicing approaches proposed in [20]—primarily focus on handling snapshot images captured using ideal filters, followed by subsequent spectral correction steps to address filter impurities.

Ideally, a Fabry-Perot filter (FPf) would efficiently transmit light within a narrow spectral range to the sensor while blocking light outside this range. However, FPf exhibit additional harmonic responses around each desired wavelength in practical implementations, as shown in Fig. 2. Moreover, snapshot spectral cameras encounter various impurities, such as spectral leaking, spectral shifting and CMOS imager variability. Therefore, they require pre-processing and post-processing steps to ensure high-quality images [21], [23]–[25].

Firstly, the incident light is conditioned using an appropriate *rejection filter* in front of the sensor to block all wavelengths outside the active range. Hence the filters will remove spectral leaking and unwanted second-order responses outside the sensor's active range [8], [24]. Secondly, *dark level correction* (or bias correction) is applied by subtracting a dark image from the SSI image to remove sensor's inherent noise and

offset. The dark reference image is usually taken when the lens is closed. Although rejection filters successfully block wavelengths outside the sensor's active range, they cannot remove some unwanted responses because they fall in the sensor's active range. These wavelengths contribute to the filter's total response and will be present in the captured data. Their contribution to the signal can be suppressed in the *spectral correction* step by using the *spectral correction matrix*, which is computed for each combination of sensor and optical components—i.e., rejection filters, light source, etc—and which is provided in the sensor calibration file [23], [26]. The correction matrix C is scene-independent and derived by minimizing the discrepancy between the actual band response—also called response matrix denoted as H—and the desired or ideal band response, denoted as H^{ideal}, i.e.,

$$\min_{C} \|H^{\text{ideal}} - C \cdot H\|_F^2, \tag{1}$$

where $\|\cdot\|_F^2$ denotes the Frobenius norm. Applying the correction matrix requires the calculation of the reflectance using a white reference [24]. However, Vunckx and Charle [25] have recently proposed an approach to enable spectral correction of raw, dark-corrected data.

Notably, the response matrix, which forms the foundation of our proposed framework, can be considered the model of the sensor and is the primary source of information about the filters on the sensor. Specific filter characteristics, such as first and second-order responses and the full width of the response peaks at half the maximum of the peak (FWHM), are extracted from the response matrix. Multiplying this matrix with an irradiance spectrum results in the simulated sensor response. In our experiments, we utilize this response matrix to simulate real-world scenarios, enabling us to evaluate the performance and effectiveness of our approach under realistic conditions.

Angularity correction proposed by Goossens *et al.* [27] addresses variability caused by incident light angles that can cause undesired spectral shifts of the measured spectra. It requires knowledge about the f-number of the lens and the distance between the lens's exit pupil and the image sensor. Then the shift in wavelength can be calculated for each position of the filters. Finally, the lens can also cause a spatially variant pixel response due to vignetting, and the pixel response of a CMOS imager can vary slightly across the sensor. *Non-uniformity correction* is applied to overcome these issues by dividing the reconstructed cube point-by-point by a non-uniformity correction cube. The computation of the latter requires an extra calibration measurement to be performed in the lab with an integrating sphere or a white reflectance tile and the whole system as (it will be) used later, i.e., with the same lens and f-number [25]. Fig. 3 shows the processing pipeline of the SSI images with the steps mentioned above. It is important to note that some of these steps are optional and can be adapted based on specific requirements. For instance, using white reference and black reference is essential to obtain reflectance values. However, these steps can be deleted if radiance values suffice for the intended analysis. Similarly, angularity correction has its applicability tied to the availability of the f-number of the optics. This correction is most relevant for fixed lenses, excluding those with autofocus mechanisms. Furthermore, the correction for non-uniformity in pixel response could be postponed after the unmixing process as it does not influence abundance estimation.

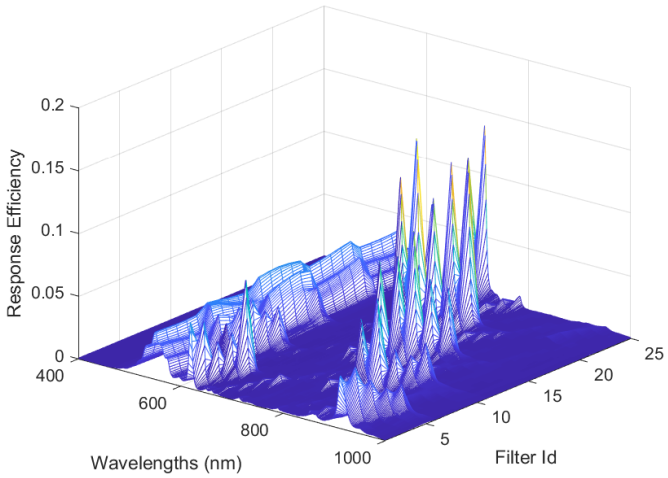

Fig. 2. The spectral response of the 25 spectral filters of the 5×5 mosaic Photon Focus SSI camera covers the wavelength range from 400 to 1000 nm. [28].

Deconvolution methods in hyperspectral imaging aim to mitigate the blurring effects and enhance spatial resolution. By estimating the imaging system's point spread function (PSF) or impulse response, deconvolution algorithms aim to reverse the blurring process and recover sharper and more accurate representations of the original scene [29], [30]. This can lead to improved spatial details, better discrimination of spectral features, and enhanced overall image quality. Furthermore, coupling deconvolution with unmixing was found to have better unmixing improvements. In [31], the authors proposed a sequential approach to unmix hyperspectral data that has been blurred during acquisition. The authors analyzed the effects of the observation process on the minimum-volume simplex (MVS) enclosing the data and showed that a deconvolution step is necessary to unmix the data correctly. While Jiang *et al.* [32] proposed a new approach called DecGMCA to jointly solve the blind source separation (BSS) and deconvolution problems based on sparse signal modeling and efficient alternative projected least square algorithm. They highlighted the gained enhancements on the unmixing by jointly solving BSS and deconvolution instead of considering these two problems independently. In [33], the authors proposed a joint unmixing-deconvolution (JUD) algorithm that combines supervised linear unmixing and deconvolution problems to increase the resolution of the abundance maps for industrial imaging systems. They proposed extensions to the algorithm based on Tikhonov regularization and block Tikhonov criterion.

III. Problem Statement and Assumptions

In this section, we provide a definition of the SSI acquisition system and outline the problem that we aim to address. The SSI camera acquires a two-dimensional image consisting of $m \times n$ pixels for each exposure, where m and n represent the

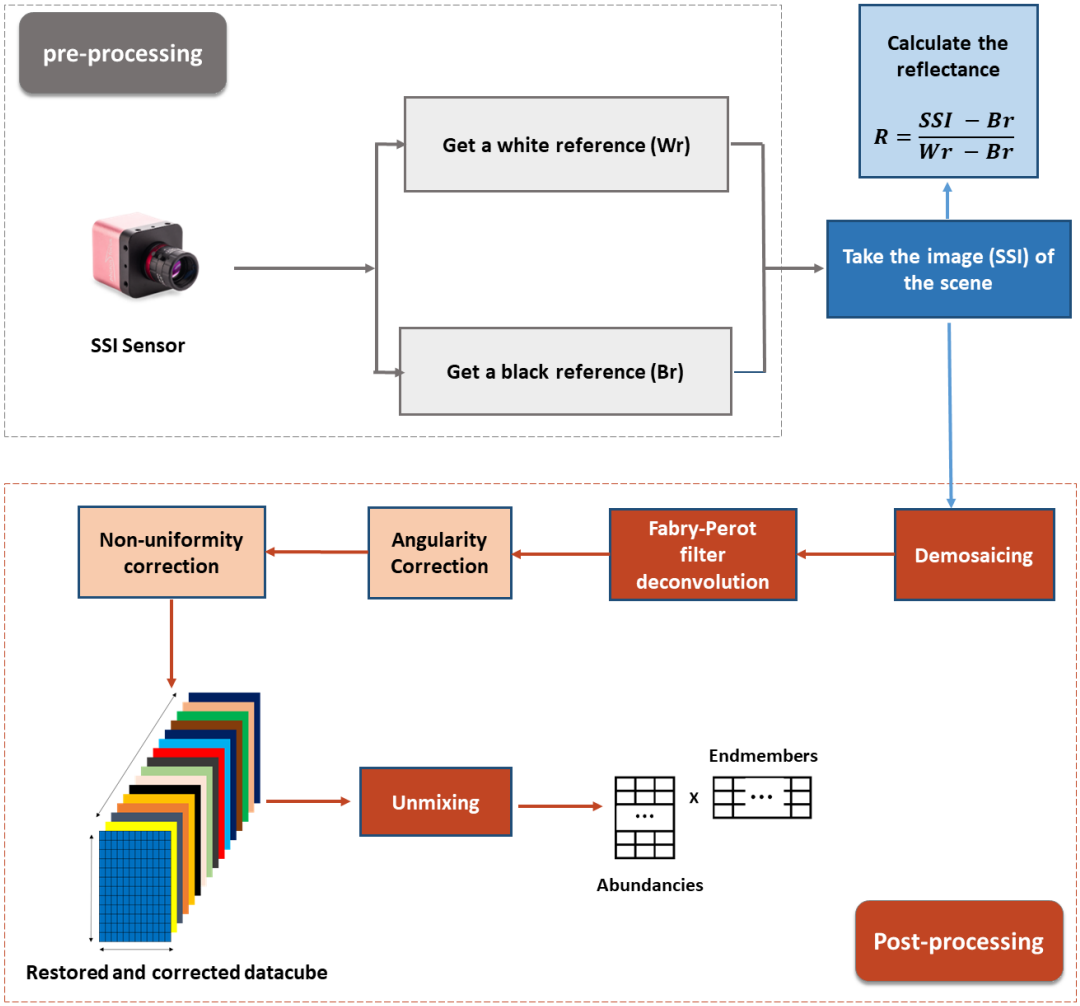

Fig. 3. Processing steps as required by the camera manufacturer to ensure high-quality snapshot spectral image restoration and unmixing.

pixel counts in the horizontal and vertical dimensions, respectively. Additionally, it is assumed that the camera observes k spectral bands. In practice, the SSI technology relies on a mosaic of Fabry-Perot filters comprised of $\sqrt{k} \times \sqrt{k}$ patches that are replicated across the sensor surface.[1]. In an ideal scenario, an FPf permits only light within a minimal spectral range to reach the sensor while blocking light outside this range. However, in real implementations, these filters exhibit additional harmonics around each wavelength of interest, as illustrated in Fig. 2. Fortunately, these filters are known and provided by the camera manufacturer [3].

For the rest of this section, our focus will be on a single patch of Fabry-Perot filters. Denoting $x_i(\lambda_i)$ as the i-th SSI pixel in the patch, which theoretically captures spectral information at λ_i nm, we have:

$$x_i(\lambda_i) = \sum_{j=1}^{k} h_i(\lambda_j) \cdot y_i(\lambda_j) + \omega_i, \tag{2}$$

[1]Typical values of k are 16 or 25, such that the patch is of size 4×4 or 5×5, respectively. Moreover, m and n are both proportional to $\sqrt{k}$. Finally, as the patch size directly equals the number of wavelength bands, k is consistently used to denote the two elements.

where $h_i(\lambda)$ represents the Fabry-Perot filter associated with Pixel i, $y_i(\lambda)$ is the actual spectrum intended to be observed by Pixel i, and ω_i denotes some additive noise. Furthermore, assuming a linear mixture model, the observed spectrum can be expressed as a combination of endmembers, i.e.,

$$y_i(\lambda) = \sum_{l=1}^{p} g_{il} f_l(\lambda), \tag{3}$$

where p represents the number of endmembers in the observed scene, $f_l(\lambda)$ signifies the spectrum of the l-th endmember, and g_{il} is the corresponding abundance proportion in Pixel i, i.e.,

$$\forall l = 1, \ldots, p,\ 0 \leq g_{il} \leq 1 \quad \text{and} \quad \sum_{l=1}^{p} g_{il} = 1. \tag{4}$$

By combining Eqs. (2) and (3), we obtain

$$x_i(\lambda_i) = \sum_{l=1}^{p} g_{il} \left(\sum_{j=1}^{k} h_i(\lambda_j) \cdot f_l(\lambda_j) \right) + \omega_i. \tag{5}$$

In this paper, we aim to estimate the p endmembers $f_l(\lambda)$ with their associated abundance coefficients g_{il} using Eqs. (5).

IV. Proposed methods

We now introduce our proposed methods. We actually propose two novel methods for SSI data exploiting the filter characteristics and using the same sparsity assumptions introduced in [20]. The latter are briefly recalled in the subsections below.

A. Clustering and Filtering-based Proposed Technique

We now introduce our approach and assumptions to solve the problem described in the previous section. Based on Eq. (2), the set of k observed SSI values and the k complete spectra of the patch can be expressed:

$$\underline{x} \triangleq \begin{bmatrix} x_1(\lambda_1), \\ \vdots \\ x_k(\lambda_k) \end{bmatrix}, \quad Y \triangleq \begin{bmatrix} y_1(\lambda_1) & \dots & y_1(\lambda_k) \\ \vdots & & \vdots \\ y_k(\lambda_1) & \dots & y_k(\lambda_k) \end{bmatrix}. \quad (6)$$

where $\underline{x}$ is defined as a k-dimensional vector representing spectral values of one SSI patch across k wavelengths, while Y is a matrix representing the full spectral values for this patch. Each row in Y corresponds to a different pixel, and each column represents a specific wavelength. The dimensions of Y are $k \times k$, where the first dimension represents the number of pixels and the second represents the number of spectral bands.

Estimating Y from $\underline{x}$ and Eq. (2) is an ill-posed problem. Therefore, we consider the same set of assumptions that we presented in the first part of this paper [20].

Assumption 1 (Pure patch assumption)**.** *For each endmember, there exists at least one sensor patch where only this endmember is present.*

In a patch where the assumption 1 is verified, the matrix Y is *approximately* rank-1 and can be replaced by a vector $\underline{y} = [y(\lambda_1), \dots, y(\lambda_k)]$ corresponding to an endmember. By noting $\underline{\omega} \triangleq [\omega_1, \dots, \omega_k]^T$ the vector associated with the noise in the patch and

$$\mathbb{H} \triangleq \begin{bmatrix} h_1(\lambda_1) & \dots & h_1(\lambda_k) \\ \vdots & & \vdots \\ h_k(\lambda_1) & \dots & h_k(\lambda_k) \end{bmatrix} \quad (7)$$

the matrix of Fabry-Perot filters (response matrix), Eq. (2) can be written as

$$\underline{x} = \mathbb{H} \cdot \underline{y}^T + \underline{\omega}, \quad (8)$$

For each patch, we first aim to recover a tentative spectrum $\underline{y}$ from Eq. (8). In practice, as the matrix $\mathbb{H}$ can be ill-conditionned[2], we aim to solve a penalized optimization problem, i.e.,

$$\min_{\underline{y} \geq 0} \frac{1}{2} \|\underline{x} - \mathbb{H} \cdot \underline{y}^T\|_2^2 + \frac{\alpha}{2} \|D \cdot \underline{y}^T\|_2^2, \quad (9)$$

where D is a square matrix that accounts for the discrete derivative of the spectrum $\underline{y}$, and α represents the penalization term. Eq (9) is a quadratic problem which can be rewritten as [34]

$$\min_{\underline{y} \geq 0} \frac{1}{2} \left\| \begin{pmatrix} \underline{x} \\ 0 \end{pmatrix} - \begin{pmatrix} \mathbb{H} \\ \sqrt{\alpha} D \end{pmatrix} \cdot \underline{y}^T \right\|_2^2. \quad (10)$$

In practice, the error value $\|\underline{x} - \mathbb{H} \cdot \underline{\hat{y}}\|_2$—where $\underline{\hat{y}}$ is the estimated spectrum obtained from Eqs. (9) or (10)—provides a measure of rank-one approximation. Indeed, if in Eq. (8) the content of Y can be approximated by a single vector, then $\|\underline{x} - \mathbb{H} \cdot \underline{\hat{y}}\|_2$ will be very low. Specifically, this means that only one endmember is present in the patch, and Assumption 1 is satisfied. However, if the error value is high, this means that multiple endmembers are present in the patch, and we must not detect the patch as pure. This brings the second assumption.

Assumption 2. *In the patches where several endmembers are present, their abundances significantly vary over each patch.*

As a consequence, when several endmemeber are present in the patch, the error value $\|\underline{x} - \mathbb{H} \cdot \underline{\hat{y}}\|_2$ will be high.

Such an error can thus be seen as a "single-source confidence measure" as proposed in KPWNMF. We thus derive from each patch one noisy estimation of one "true" endmember. The recovered spectra with low approximation error are collected and arranged in a matrix denoted $\mathbb{F}$. Then the final endmembers are estimated using *Selective* K-means or K-medians proposed in [35], initialized with K-means++ [36][3].

Once the actual endmembers are derived and stored in the matrix F, a final step involves estimating the abundance in each pixel of the SSI image. We adopt the low-rank matrix completion framework introduced in [20] for this purpose. At the patch level, we consider the observed values $y_i(\lambda_i)$ to be part of a partially observed $k \times k$ matrix Y. Denoting S as the matrix of endmembers convolved by $\mathbb{H}$, we obtain the matrix form of Eq. (5), i.e.,

$$\mathbb{H} \circ Y \approx \mathbb{H} \circ (G \cdot S), \quad (11)$$

where G is the matrix of abundances in the considered patch, and $\mathbb{H}$ is a scaled version of H. In practice, we initialize G through least-squares regression using F and the patch demosaiced by Weighted Bilinear interpolation (WB) approach [4]. Subsequently, we aggregate all these matrices Y to update the abundance matrix using Naive WNMF in [20] globally. The whole strategy is provided in Algorithm 2.

B. Method with Relaxed Abundance Sparsity Assumption

We now introduce our second approach. It may be seen as an extension of the previous one as it also assumes Assumption 1 to be valid. However, it significantly relax Assumption 2 which is replaced by the following one.

Assumption 3. *In the patches where several endmembers are present, their abundances may or may not vary over each patch.*

[2]For example, the 5×5 filter matrix $\mathbb{H}$ using real FPf in [8] has two rows which are almost null.

[3]Similarly to KPWNMF, FPKmeans utilizes K-medians clustering with the ℓ_1 norm. The clustering process is repeated 10 times, and the solution with the lowest within-cluster sums of point-to-centroid distances is selected as the optimal solution.

This assumption states that in the patches where multiple endmembers are present, we do not require any constraint on their abundances. Consequently, the approximation error $\|\underline{x}-\mathbb{H}\cdot\underline{\hat{y}}\|_2$ tends to be low when a patch is pure (in accordance with Assumption 1) or when the abundances of multiple endmembers remain consistent within the patch. However, the approximation error increases significantly in patches with multiple endmembers and their abundance proportions vary across the patch. As for FPKmeans, we collect the proportion[4] ρ of tentative endmembers in the "best" patches—i.e., those which provide the smallest approximation errors—and we arrange them in a matrix denoted $\mathbb{Y}$. As explained above, each row vector of this matrix is either an estimate of an endmember of F or a mixture of them. As we assumed a linear mixture model (LMM), this matrix can be written as

$$\mathbb{Y} = \mathbb{G} \cdot F. \tag{12}$$

Then, as we did in VPWNMF in the fist part of this paper [20], VCA is used to extract the final set of endmembers. Finally, the abundance matrix G is estimated using the same approach as in FPKmeans. The whole strategy is provided in Algorithm Algorithm 3.

C. Algorithms

This section introduces the pseudo code for our proposed methods. While these algorithms share several procedural steps, they fundamentally differ in their methodologies as previously discussed. Algorithm 1 introduces the shared patch processing steps essential to both the Filter Patch-based Kmeans (FPKmeans) and the Filter Patch-based Vertex Component Analysis (FPVCA), focusing on the extraction of tentative endmembers. Building upon this, Algorithm 2 and Algorithm 3 diverge to apply specific endmember extraction techniques, and the usage of Assumption 2 or Assumption 3.

V. Experiments and Results

A. Experiment Setup

To evaluate the effectiveness of our proposed methods, we conducted experiments on synthetic images and real snapshot spectral imaging (SSI) images captured by SSI cameras. We utilized the same set of images introduced in Part I of our study for the synthetic images. Specifically, we considered two scenarios: Assumptions one and two are satisfied Fig. 4, and Assumptions one and three are satisfied Fig. 5. Each synthetic image consisted of a 100×100 pixel grid with three endmembers, namely water, metal, and concrete, whose spectral signatures were obtained from [37]. Furthermore, we consider the real spectral profiles derived from the calibration files of the photonfocus Snapshot 5x5 spectral camera [28]. Spectral correction is applied after processing the images using the correction matrix provided by the camera manufacturer, as explained in Section II.

In our evaluation, we compared the performance of our approaches against several baseline methods, including the

[4]As for KPWNMF, we only keep spectra estimated in patches where the approximation error is below the median of all the patch norm errors, i.e., $\rho = 0.5$.

Algorithm 1 Rank-one patch detection and spectra estimation method used in both proposed FPKmeans and FPVCA

Inputs:
The SSI matrix
p: the number of endmembers
$\mathbb{H}$: the response matrix
α: the regularization parameter
nb_patches: the number of patches to be processed

Output:
- Matrix $\mathbb{M}$ containing the "best" vectors for further processing.

Processing:
1: **for** $r = 1$ **to** nb_patches **do**
2: Let $\underline{x}_r$ be the SSI vector linked to Patch r
3: Estimate $\underline{\hat{y}}$ using Eq (10)
4: **end for**
5: Keep the 50% best vectors $\underline{\hat{y}}$—according to $\|\underline{x}_r - \mathbb{H}\underline{\hat{y}}\|_2$—and organize them as a matrix $\mathbb{M}$
6: **return** $\mathbb{M}$

Algorithm 2 Filter Patch-based Kmeans (resp. K-medians), (FPKmeans)

Inputs:
Matrix $\mathbb{F}$ from Algorithm 1
p: the number of endmembers

Outputs:
$[G, F]$ represents the final abundances and endmembers.

Processing:
1: Call Algorithm 1 to obtain $\mathbb{F}$
2: $F = \text{K-means}(\mathbb{F}, p)$ (resp. K-medians$(\mathbb{F}, p)$)
3: **Compute** G using Eq. (11) and Naive WNMF

Algorithm 3 Filter Patch-based Vertex Component Analysis (FPVCA)

Inputs:
Matrix $\mathbb{Y}$ from Algorithm 1
p: the number of endmembers

Outputs:
$[G, F]$ represents the final abundances and endmembers.

Processing:
1: Call Algorithm 1 to obtain $\mathbb{Y}$
2: $F = \text{VCA}(\mathbb{Y}, p)$
3: **Compute** G using equation (11) and Naive WNMF

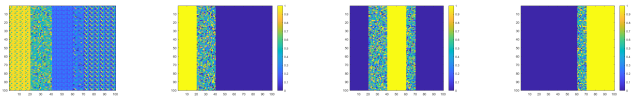

(a) SSI Image (b) Water (c) Metal (d) Concrete

Fig. 4. Image 1, SSI image where assumptions 1 and assumption 2 are satisfied with abundance maps of the three endmembers.

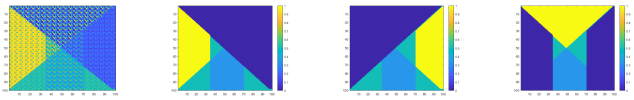

(a) SSI Image (b) Water (c) Metal (d) Concrete

Fig. 5. Image 2, SSI image where assumptions 1 and assumption 3 are satisfied with abundance maps of the three endmembers.

Naive method, KPWNMF, VPWNMF, and five two-step demosaicing-then-unmixing methods. For the latter category, we employed seven state-of-the-art demosaicing methods, namely GRMR [8], BTES [7], WB [4], PPID [6], ItSD [5], SAND [9], and PCWB [38]. In the second step, we unmix the restored data cube Y using VCA for estimating the endmembers and Fully Constrained Least Squares (FCLS) for abundance estimation. It is important to note that in these experiments, we consider a more complex scenario by simulating realistic filter responses. As a result, unlike the first part of this paper, an extra stage is introduced for all the state-of-the-art (SotA) methods. This additional step involves applying the correction matrix. We have two options for its placement: either after the demosaicing step or equivalently after the unmixing step. However, for consistency and to maximize performance, we apply the correction matrix after demosaicing for all methods because they perform better except PPID, KPWNMF, and VPWNMF, which show similar performance trends in both placements. We evaluated the tested methods by assessing demosaicing and unmixing enhancements. For demosaicing, we measured the performance using Peak Signal-to-Noise Ratio (PSNR) by comparing estimated Y matrices with ground truth. While for unmixing, we utilized Signal-to-Interference Ratio (SIR) and Spectral Angle Mapper (SAM) for endmember estimation, along with Mixing Error Ratio (MER) for quantifying abundance map quality. We additionally incorporated RMSE for abundance estimation accuracy and running time in seconds to assess computational efficiency.

We also conducted experiments to study the impact of regularization parameter in the deconvolution step on the effectiveness of the proposed methods.

For our real data experiment, we use images from the Hyko 2 dataset [21]. This dataset consists of images captured by two snapshot mosaic cameras and covers the spectral range from 400 to 1000 nm, encompassing the visible and near-infrared regions.

B. The impact of Regularization Parameter α

In the first set of experiments we study the impact of the regularization on the deconvolution performance. The regularization parameter α controls the Tikhonov regularization

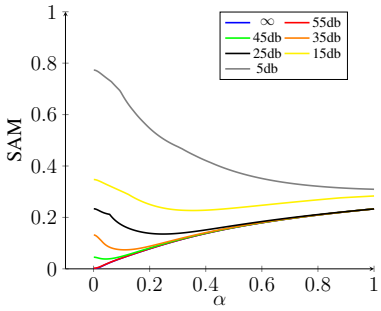

Fig. 6. Influence of the regularization parameter α on the achieved Spectral Angle Mapper (SAM) value for each noise level

in Eq. (9) , which helps balance the trade-off between data fidelity and regularization in the deconvolution process. Fig.6 shows the influence of the regularization parameter α on the achieved Spectral Angle Mapper (SAM) value for each noise level in the context of the inverse problem when applied to noiseless and noisy scenarios. We can see from the figure that a small value of $\alpha = 0.0005$ results in the best SAM value. However, as noise is introduced, the regularization parameter needs to be increased to improve the robustness of the deconvolution process. This trend can be followed in the plot, where higher noise levels correspond to larger values of α for achieving better SAM. It is important to note that in all the following experiments in the article, 0.0005 was chosen as the value for α for the noiseless case. For the noisy case, we selected the value from the figure where SAM was the lowest, ensuring optimal performance at each noise level.

C. Performance evaluation on synthetic images for the real case

In the second set of experiments, we utilize images introduced in Part I of our study. We consider a real filter with a 5×5 filter pattern and investigate the performance of the tested methods under different noise levels. The PSNR, SAM, SIR, and SAM achieved by all the methods are reported in Table II. While the average performance with different noise levels for both images with is presented in Fig. 7 and Fig. 8 respectively. The results presented in the table and figures reveal several significant observations:

- The performance of both KPWNMF and VPWNMF methods drops when compared to the ideal situation. This decline is mainly due to two reasons: first, the spectral correction step, which causes estimation mistakes, especially when there is a lot of background noise. Second, the weight matrix uses its values from the response matrix during the factorization step for each rank-1 patch.
- The proposed FPKmeans and FPVCA methods exhibit superior performance in PSNR compared to our previous methods and the two-step approaches. The performance of these methods may vary under different noise levels. FPKmeans and FPVCA consistently outperform the other methods. However, their performance declines at lower input SNRs, and they exhibit similar demosaicing performance to the state-of-the-art methods. It is worth

TABLE II
PSNR, SAM, SIR, MER,RMSE, AND TIME IN SECONDS OBTAINED FOR THE SYNTHETIC IMAGES WITH 5X5 REAL FILTERS. IN BOLD, THE HIGHEST PERFORMANCE VALUE.

Method	Image 1 (Assumptions 1 & 2)						Image 2 (Assumptions 1 & 3)					
	PSNR	SAM	SIR	MER	RMSE	Time	PSNR	SAM	SIR	MER	RMSE	Time
GMRM	23.0	0.52	8.3	0.7	0.4	1.7	24.3	0.36	10.8	0.2	0.4	1.6
BTES	18.6	0.52	9.4	-6.1	0.5	**0.3**	18.3	0.3	8.4	-3.3	0.5	0.5
WB	23.8	0.38	13.5	-4.2	0.4	**0.3**	26.4	0.3	16.4	-0.3	0.3	**0.4**
PPID	28.6	0.12	23.2	7.1	0.3	0.4	33.9	0.1	30.2	13.0	0.2	**0.4**
ItSD	24.4	0.32	11.8	0.2	0.5	**0.3**	26.3	0.32	14.3	0.6	0.4	**0.4**
SAND	28.9	0.13	24.3	7.9	0.3	3728	33.9	0.1	17.3	9.1	0.2	3700
PCWB	27.3	0.15	19	5.3	0.3	0.3	29.3	0.4	15	2.3	0.2	0.3
Naive	23.9	0.4	11.2	2.5	0.3	10	25.6	0.4	12.0	3.0	0.3	10
KPWNMF	**30.1**	0.06	32.7	**12.5**	0.2	6.1	34.9	0.08	32.2	16.4	0.2	6.1
VPWNMF	30.0	0.06	33.6	12.4	0.2	5.1	**35.6**	0.06	33.1	16.9	0.2	5.1
FPVCA	**30.1**	$9 \cdot 10^{-8}$	**149.0**	12.2	**0.1**	4	**36.5**	$8 \cdot 10^{-8}$	**149.0**	**17.6**	**0.07**	4
FPKmeans	**30.1**	$9 \cdot 10^{-8}$	**149.0**	12.2	**0.1**	4.5	35.8	0.05	104.5	17.1	**0.07**	4.5

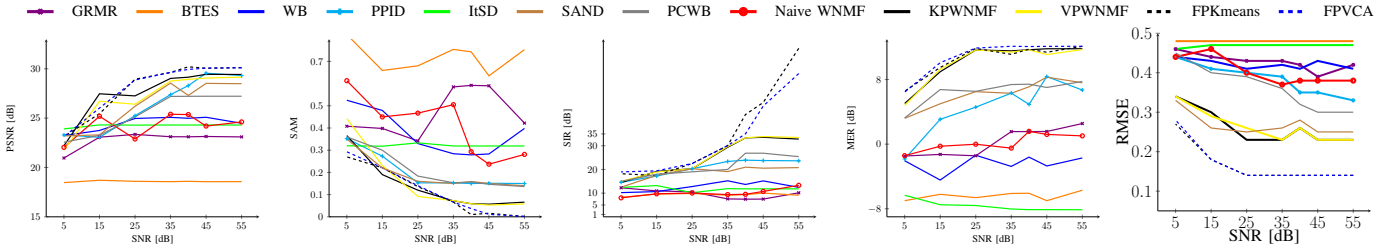

Fig. 7. From left to right: mean PSNR, SAM, SIR, MER and RMSE—obtained for Image 1 (Assumption 1&2) with 5×5 real filter—relative to input SNR.

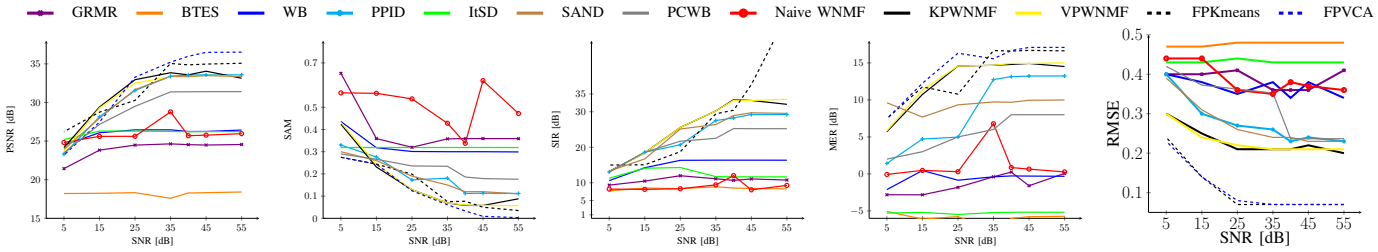

Fig. 8. From left to right: mean PSNR, SAM, SIR, MER and RMSE—obtained for Image 2 (Assumption 1&3) with 5×5 Real filter—relative to input SNR.

mentioning that the advantage of FPKmeans and FPVCA is that they eliminate the need for spectral correction steps required in the other methods.

- In addition to their superior reconstruction quality, the proposed FPKmeans and FPVCA methods outperform all other methods regarding endmember identification. They achieve the lowest spectral angle mapper (SAM) values and the highest signal interference ratio (SIR) values, indicating their accurate identification of endmembers even in the presence of noise. Figures 9 and 10 illustrate the comparison of true and estimated endmembers using a 5×5 filter in the noiseless case. These methods exhibit robustness to noise, maintaining their superior performance even at higher noise levels. However, it is worth noting an exception observed in Image 2 with SNRs below 25 dB, where even PPID outperforms FPKmeans in terms of SIR. In the case of Image 1, where the assumptions of FPKmeans are satisfied, the latter exhibits slightly better performance than FPVCA.
- The proposed methods FPKmeans and FPVCA demonstrate comparable performance in terms of the Mixing Error Ratio (MER), to the joint unmixing and demosaicing approaches KPWNMF and VPWNMF. These methods consistently achieve the highest MER values among all other methods, indicating their superior accuracy in estimating the abundance maps. Furthermore, the experiments reveal the robustness of FPKmeans and FPVCA to noise, as they maintain their exceptional performance even at higher noise levels. Fig. 11 and Fig. 12 illustrate the comparison between the restored abundance maps and the true abundance maps for both images, using the 5×5 filter in the noiseless case.
- The RMSE results, implying precision in abundance estimation, show FPKmeans and FPVCA as superior, even under various noise levels. Their lowest RMSE values, complemented by the visual quality of abundance maps in figures Fig. 11 and Fig. 12 , demonstrate their robustness and accuracy.
- In assessing the new methods FPKmeans and FPVCA, we note their computational time is improved compared to

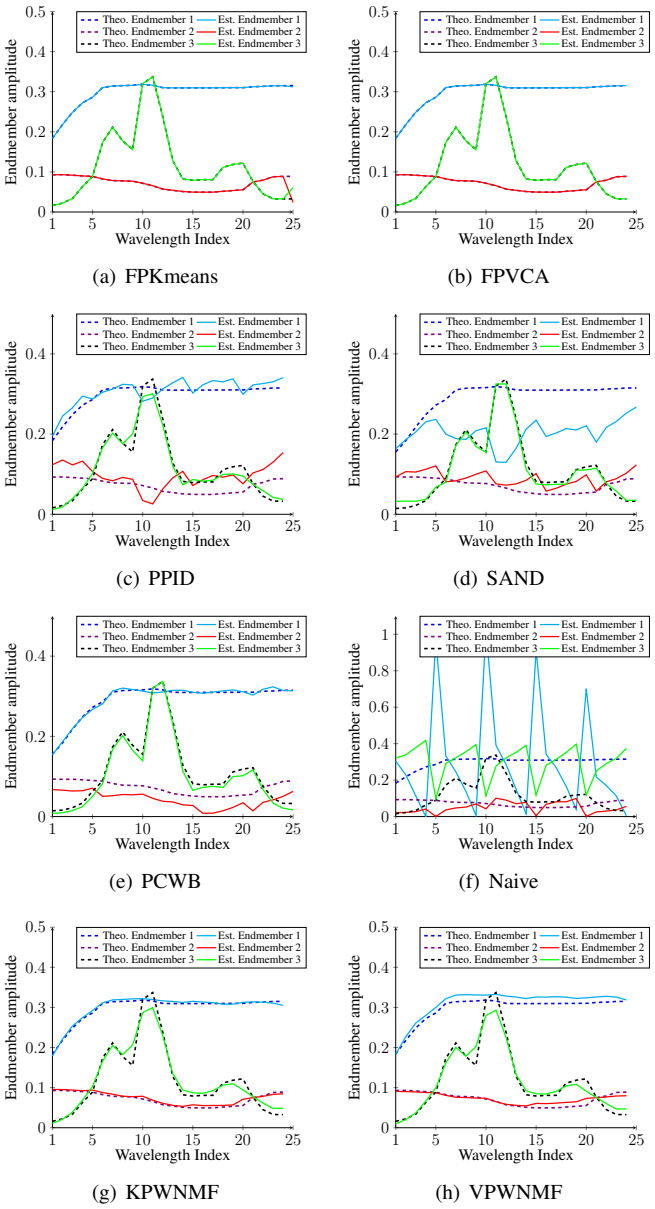

(a) FPKmeans (b) FPVCA (c) PPID (d) SAND (e) PCWB (f) Naive (g) KPWNMF (h) VPWNMF

Fig. 9. Estimated spectra for the Image 1 with Real filter of size 5×5.

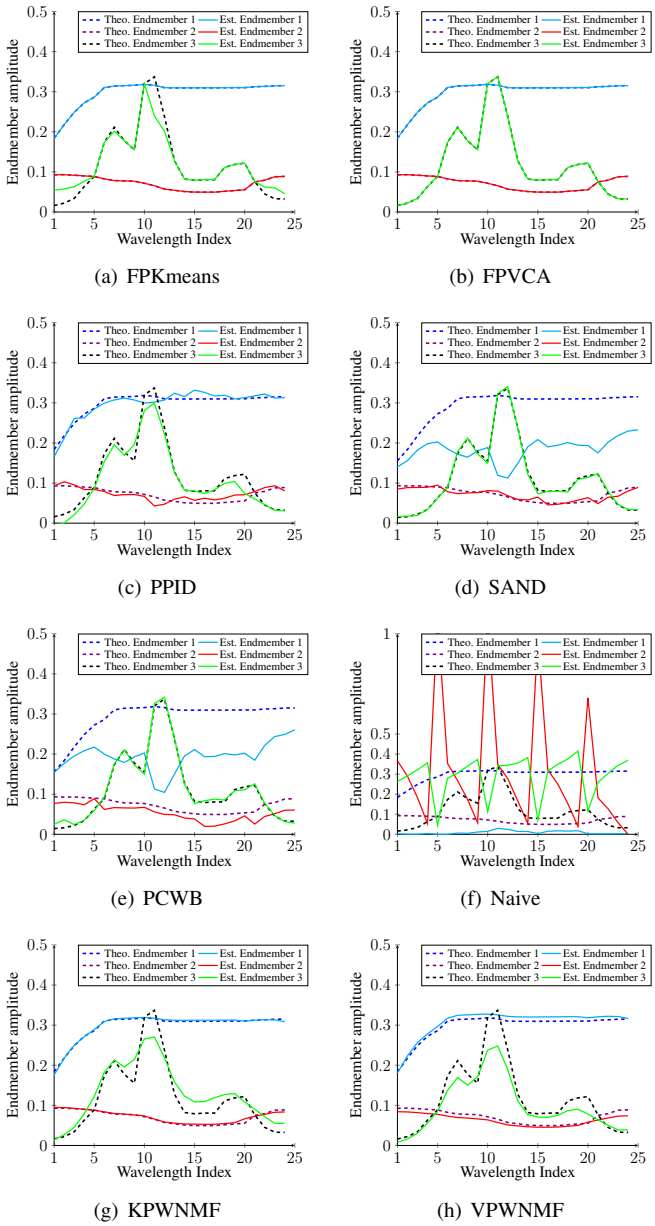

(a) FPKmeans (b) FPVCA (c) PPID (d) SAND (e) PCWB (f) Naive (g) KPWNMF (h) VPWNMF

Fig. 10. Estimated spectra for the Image 2 with Real filter of size 5×5.

KPWNMF and VPWNMF. However, it remains higher than some SotA methods. Despite this, our study focuses on demonstrating the accuracy and effectiveness of these methods in snapshot spectral imaging rather than on computational efficiency. Optimizing running time is considered future work to enhance these methods for more time-sensitive applications

D. Performance evaluation on Hyko 2 dataset

In the first part of the journal, the Hyko dataset was utilized to evaluate various methods for image segmentation, including VPWNMF and KPWNMF. The results demonstrated that VPWNMF achieved the best segmentation performance, followed by KPWNMF. Spectral correction was applied to the output of these methods after the demosaicing step to improve the accuracy[5]. In the second part of the journal, a similar experiment was conducted using the same dataset. However, in this case, the proposed methods, FPVCA, and FPKmeans, exhibited comparable performance to VPWNMF and KPWNMF, respectively, without spectral correction. The results in Fig. 13 showed that FPVCA exhibited comparable performance to VPWNMF, while FPKmeans outperformed all other methods, including VPWNMF. It is worth noting that the spectral correction step did not affect the abundance estimation for VPWNMF, and KPWNMF as their abudndances remained consistent even without correction.

[5]The correction matrix was kindly provided to us by the Hyko 2 dataset authors.

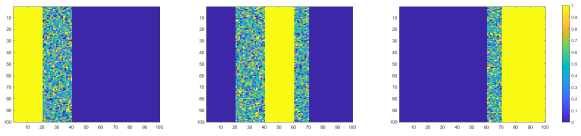

(a) Ground truth

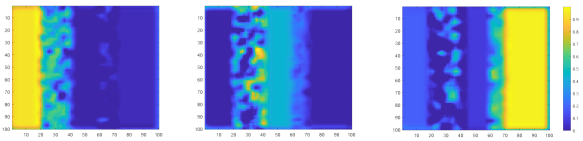

(b) PPID

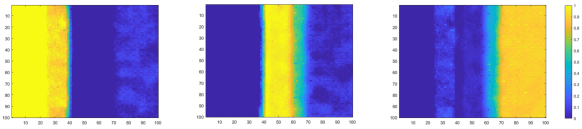

(c) SAND

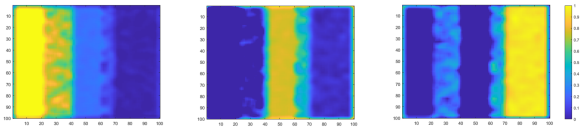

(d) PCWB

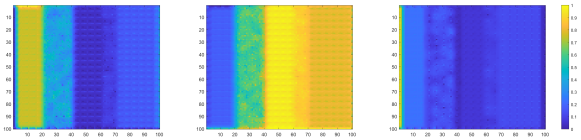

(e) Naive

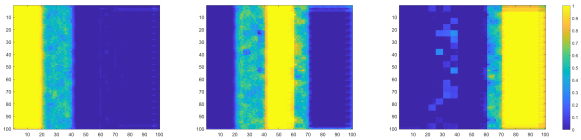

(f) KPWNMF

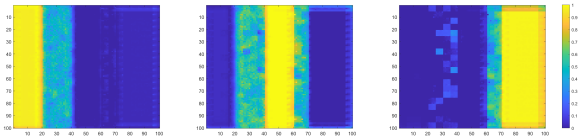

(g) VPWNMF

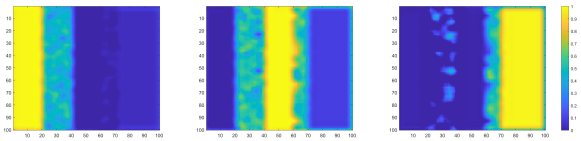

(h) FPVCA

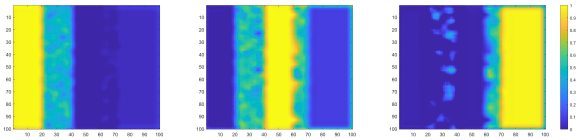

(i) FPKmeans

Fig. 11. Estimated abundance maps for the Image 1 with real filter of size 5×5

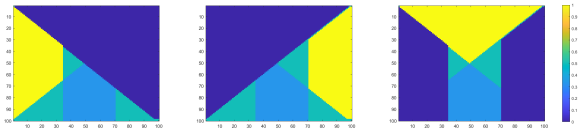

(a) Ground truth

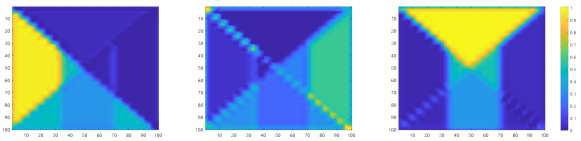

(b) PPID

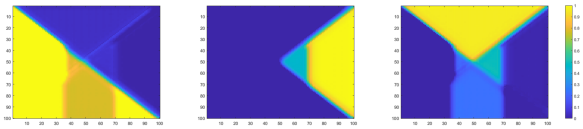

(c) SAND

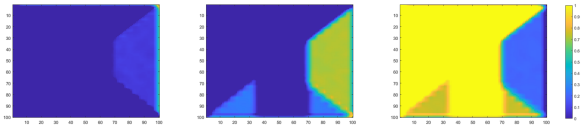

(d) PCWB

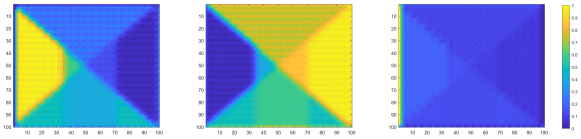

(e) Naive

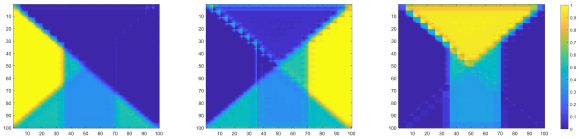

(f) KPWNMF

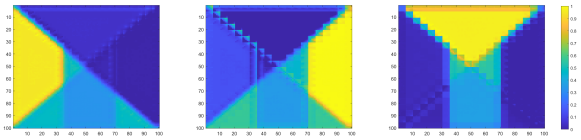

(g) VPWNMF

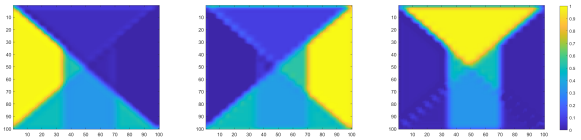

(h) FPVCA

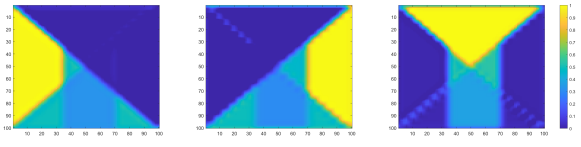

(i) FPKmeans

Fig. 12. Estimated abundance maps for the Image 2 with real filter of size 5×5

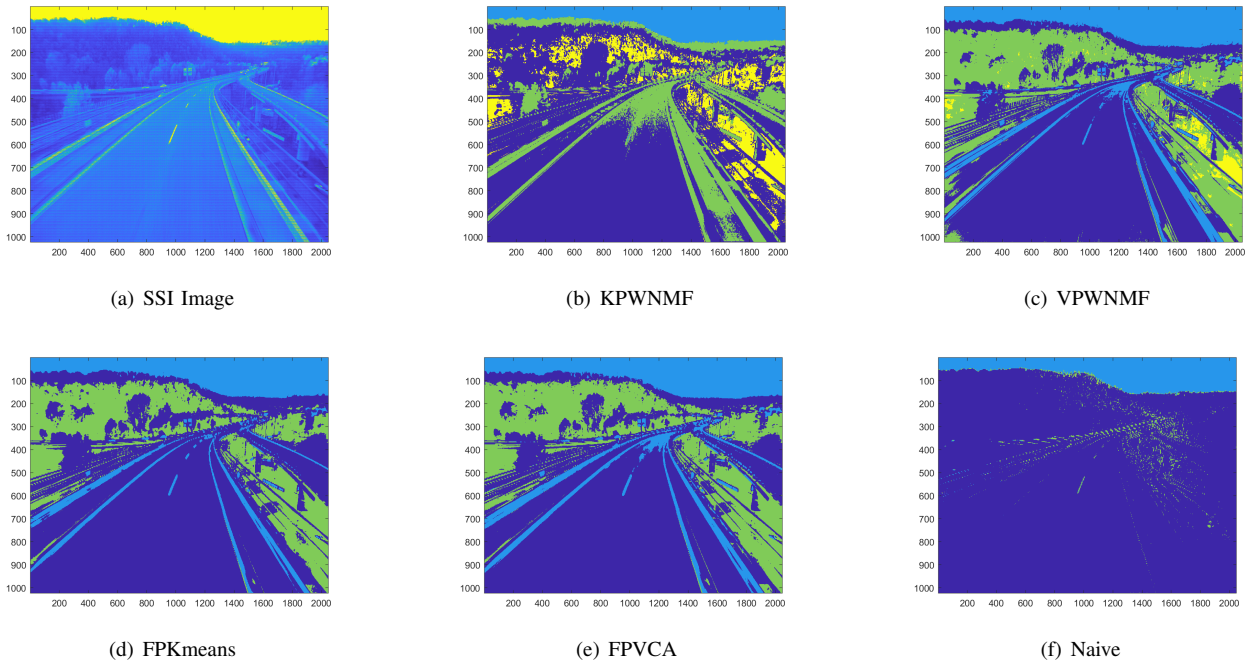

(a) SSI Image (b) KPWNMF (c) VPWNMF

(d) FPKmeans (e) FPVCA (f) Naive

Fig. 13. Comparison of the segmentation performance of all the methods on the Hyko 2 Dataset Image

VI. Conclusion and Discussion

In the second part of this work, we study the significance of joint deconvolution and unmixing for snapshot spectral imaging (SSI). The experimental results on synthetic and real data demonstrated that the proposed methods, FPVCA, and FPKmeans, outperformed the joint demosaicing and unmixing approaches and the traditional 2-stage methods involving separate demosaicing and unmixing steps. Moreover, integrating deconvolution into the processing pipeline yielded superior results, enhancing the accuracy of image segmentation, demosaicing, and unmixing accuracy. The improved performance is attributed to the proposed sparsity assumptions and utilizing the harmonics of the Fabry-Perot filters (FPf) provided in the response matrix. This approach eliminated the need for spectral correction steps after the demosaicing process, simplifying the workflow and improving efficiency. However, it is essential to acknowledge the existing challenges, such as spectral variability, which can still introduce estimation errors. Future work will address these challenges and further refine the methods to tackle spectral variability and enhance the overall performance of snapshot spectral imaging systems. Additionally, incorporating models for spectral correction based on varying optical setups and light sources will be explored to extend the generalizability of our methods in diverse practical scenarios. Finally, we will optimize the running time of our methods to ensure their applicability in time-sensitive scenarios.

Acknowledgement

The authors would like to acknowledge the anonymous reviewers for their valuable comments to improve the present work.

References

[1] J. G. Michael West and C. Galvan, "Commercial snapshot spectral imaging: The art of the possible." Available online at https://www.mitre.org/sites/default/files/publications/pr-18-3832-commercial-snapshot-spectral-imaging-art-of-possible.pdf. Last access: 08/26/2022., 2018.

[2] B. Geelen, N. Tack, and A. Lambrechts, "A compact snapshot multispectral imager with a monolithically integrated per-pixel filter mosaic," in *Advanced Fabrication Technologies for Micro/Nano Optics and Photonics VII* (G. von Freymann, W. V. Schoenfeld, and R. C. Rumpf, eds.), SPIE, Mar. 2014.

[3] B. Geelen, C. Blanch, P. Gonzalez, N. Tack, and A. Lambrechts, "A tiny VIS-NIR snapshot multispectral camera," in *Advanced Fabrication Technologies for Micro/Nano Optics and Photonics VIII* (G. von Freymann, W. V. Schoenfeld, R. C. Rumpf, and H. Helvajian, eds.), SPIE, Mar. 2015.

[4] J. Brauers and T. Aach, "A color filter array based multispectral camera," in *12. Workshop Farbbildverarbeitung* (G. C. Group, ed.), (Ilmenau), October 5-6 2006.

[5] J. Mizutani, S. S. Ogawa, K. Shinoda, M. Hasegawa, and S. Kato, "Multispectral demosaicking algorithm based on inter-channel correlation," in *Proc. IEEE VCIP'14*, pp. 474–477, 2014.

[6] S. Mihoubi, O. Losson, B. Mathon, and L. Macaire, "Multispectral demosaicing using pseudo-panchromatic image," *IEEE Trans. Comput. Imaging*, vol. 3, pp. 982–995, Dec. 2017.

[7] L. Miao, H. Qi, R. Ramanath, and W. Snyder, "Binary tree-based generic demosaicking algorithm for multispectral filter arrays," *IEEE Trans. Image Process.*, vol. 15, pp. 3550–3558, Nov. 2006.

[8] G. Tsagkatakis, M. Bloemen, B. Geelen, M. Jayapala, and P. Tsakalides, "Graph and rank regularized matrix recovery for snapshot spectral image demosaicing," *IEEE Trans. Comput. Imaging*, vol. 5, pp. 301–316, June 2019.

[9] L. Bian, Y. Wang, and J. Zhang, "Generalized MSFA engineering with structural and adaptive nonlocal demosaicing," *IEEE Trans. Image Process.*, vol. 30, pp. 7867–7877, 2021.

[10] K. Dijkstra, J. van de Loosdrecht, L. R. B. Schomaker, and M. A. Wiering, "Hyperspectral demosaicking and crosstalk correction using deep learning," *Machine Vision and Applications*, vol. 30, pp. 1–21, July 2018.

[11] T. A. Habtegebrial, G. Reis, and D. Stricker, "Deep convolutional networks for snapshot hypercpectral demosaicking," in *Proc. IEEE WHISPERS'19*, Sept. 2019.

[12] Z. Pan, B. Li, H. Cheng, and Y. Bao, "Joint demosaicking and denoising for CFA and MSFA images using a mosaic-adaptive dense residual network," in *Computer Vision – ECCV 2020 Workshops*, pp. 647–664, Springer International Publishing, 2020.
[13] K. Feng, Y. Zhao, J. C.-W. Chan, S. Kong, X. Zhang, and B. Wang, "Mosaic convolution-attention network for demosaicing multispectral filter array images," *IEEE Trans. Comput. Imaging*, vol. 7, pp. 864–878, 2021.
[14] J. M. P. Nascimento and J. M. Bioucas-Dias, "Vertex component analysis: a fast algorithm to unmix hyperspectral data," *IEEE Trans. Geosci. Remote Sens.*, vol. 43, no. 4, pp. 898–910, 2005.
[15] M. E. Winter, "N-FINDR: An algorithm for fast autonomous spectral end-member determination in hyperspectral data," in *Imaging Spectrometry V*, vol. 3753, pp. 266–275, International Society for Optics and Photonics, 1999.
[16] J. M. Bioucas-Dias, A. Plaza, N. Dobigeon, M. Parente, Q. Du, P. Gader, and J. Chanussot, "Hyperspectral unmixing overview: Geometrical, statistical, and sparse regression-based approaches," *IEEE J. Sel. Topics Appl. Earth Observ. Remote Sens.*, vol. 5, pp. 354–379, Apr. 2012.
[17] Y. Deville, "Sparse component analysis: A general framework for linear and nonlinear blind source separation and mixture identification," in *Blind Source Separation*, pp. 151–196, Springer, 2014.
[18] A. Boulais, O. Berné, G. Faury, and Y. Deville, "Unmixing methods based on nonnegativity and weakly mixed pixels for astronomical hyperspectral datasets," *Astronomy & Astrophysics*, vol. 647, p. A105, mar 2021.
[19] F. Movahedi Naini, G. Hosein Mohimani, M. Babaie-Zadeh, and C. Jutten, "Estimating the mixing matrix in sparse component analysis (sca) based on partial k-dimensional subspace clustering," *Neurocomputing*, vol. 71, no. 10, pp. 2330–2343, 2008.
[20] K. Abbas, M. Puigt, G. Delmaire, and G. Roussel, "Locally-rank-one joint unmixing and demosaicing methods for snapshot spectral images. part I: a low-rank completion-based framework." Preprint, 2023.
[21] C. Winkens, F. Sattler, V. Adams, and D. Paulus, "HyKo: A spectral dataset for scene understanding," in *Proc. IEEE ICCVW'17*, IEEE, Oct. 2017.
[22] K. Abbas, M. Puigt, G. Delmaire, and G. Roussel, "Filtering-based endmember identification method for snapshot spectral images," in *Proc. IEEE WHISPERS'22*, (Roma, Italy), Sept. 2022.
[23] F. Xiong, J. Zhou, and Y. Qian, "Material based object tracking in hyperspectral videos," *IEEE Transactions on Image Processing*, vol. 29, pp. 3719–3733, 2020.
[24] IMEC, "Hyperspectral sensors user manual." Available online at Support Portal of imec https://www.imec-int.com/, 2019.
[25] K. Vunckx and W. Charle, "Accurate video-rate multi-spectral imaging using imec snapshot sensors," in *Proc. IEEE WHISPERS'21*, pp. 1–7, 2021.
[26] J. Pichette, T. Goossens, K. Vunckx, and A. Lambrechts, "Hyperspectral calibration method For CMOS-based hyperspectral sensors," in *Photonic Instrumentation Engineering IV* (Y. G. Soskind and C. Olson, eds.), vol. 10110, p. 101100H, International Society for Optics and Photonics, SPIE, 2017.
[27] T. Goossens, K. Vunckx, A. Lambrechts, and C. V. Hoof, "Spectral shift correction for fabry-perot based spectral cameras," in *Proc. IEEE WHISPERS'19*, IEEE, Sept. 2019.
[28] Photonfocus, "Photonfocus snapshot mosaic camera cmv2k-sm5x5." https://www.photonfocus.com/products/camerafinder/camera/mv0-d2048x1088-c01-hs02-160-g2/, Last accessed: 2023-08-07.
[29] X. Wang, J. Chen, and C. Richard, "Tuning-free plug-and-play hyperspectral image deconvolution with deep priors," *IEEE Transactions on Geoscience and Remote Sensing*, vol. 61, pp. 1–13, 2023.
[30] R. Abi Rizk, F. Orieux, and A. Abergel, "Super-Resolution Hyperspectral Reconstruction with Majorization-Minimization Algorithm and Low-Rank Approximation," *IEEE Transactions on Computational Imaging*, 2022.
[31] S. Henrot, C. Soussen, and D. Brie, "Sequential deconvolution - Unmixing of blurred hyperspectral data," in *IEEE International Conference on Image Processing, ICIP 2014*, (Paris, France), Oct. 2014. Simon Henrot est au GIPSA-lab depuis février 2014; cet article est lié à sont travail de thèse au CRAN.
[32] M. Jiang, J. Bobin, and J.-L. Starck, "Joint multichannel deconvolution and blind source separation," *SIAM Journal on Imaging Sciences*, vol. 10, pp. 1997–2021, jan 2017.
[33] Y. Song, E.-H. Djermoune, D. Brie, and C. Richard, "Joint unmixing-deconvolution algorithms for hyperspectral images," in *27th European Signal Processing Conference, EUSIPCO 2019*, (Coruna, Spain), Sept. 2019.
[34] P. Chatelain, G. Delmaire, M. Puigt, and G. Roussel, "Inversion de réseaux de filtres de Fabry-Perot pour la restauration de cubes hyperspectraux," in *Actes du GRETSI*, (Nancy, France), Sept. 2022.
[35] M. Puigt and Y. Deville, "Iterative-shift cluster-based time-frequency BSS for fractional-time-delay mixtures," in *Proc. ICA'09*, pp. 306–313, 2009.
[36] D. Arthur and S. Vassilvitskii, "K-means++: The advantages of careful seeding," in *Proc. SODA'07*, p. 1027–1035, SIAM, 2007.
[37] "U.S. Geological Survey (USGS) spectral library." https://www.usgs.gov/labs/spectroscopy-lab/science/spectral-library, Last accessed: 2022-10-24.
[38] V. Rathi and P. Goyal, "Convolution filter based efficient multispectral image demosaicking for compact msfas.," in *VISIGRAPP (4: VISAPP)*, pp. 112–121, 2021.